

Unveiling interatomic distances influencing the reaction coordinates in alanine dipeptide isomerization: An explainable deep learning approach

Kazushi Okada,¹ Takuma Kikutsuji,¹ Kei-ichi Okazaki,^{2,3,a)} Toshifumi Mori,^{4,5,b)} Kang Kim,^{1,c)} and Nobuyuki Matubayasi^{1,d)}

¹⁾Division of Chemical Engineering, Department of Materials Engineering Science, Graduate School of Engineering Science, Osaka University, Toyonaka, Osaka 560-8531, Japan

²⁾Research Center for Computational Science, Institute for Molecular Science, Okazaki, Aichi 444-8585, Japan

³⁾Graduate Institute for Advanced Studies, SOKENDAI, Okazaki, Aichi 444-8585, Japan

⁴⁾Institute for Materials Chemistry and Engineering, Kyushu University, Kasuga, Fukuoka 816-8580, Japan

⁵⁾Interdisciplinary Graduate School of Engineering Sciences, Kyushu University, Kasuga, Fukuoka 816-8580, Japan

(Dated: 25 April 2024)

The present work shows that the free energy landscape associated with alanine dipeptide isomerization can be effectively represented by specific interatomic distances without explicit reference to dihedral angles. Conventionally, two stable states of alanine dipeptide in vacuum, *i.e.*, $C7_{\text{eq}}$ (β -sheet structure) and $C7_{\text{ax}}$ (left handed α -helix structure), have been primarily characterized using the main chain dihedral angles, φ (C-N-C $_{\alpha}$ -C) and ψ (N-C $_{\alpha}$ -C-N). However, our recent deep learning combined with “Explainable AI” (XAI) framework has shown that the transition state can be adequately captured by a free energy landscape using φ and θ (O-C-N-C $_{\alpha}$) [T. Kikutsuji, *et al. J. Chem. Phys.* **156**, 154108 (2022)]. In perspective of extending these insights to other collective variables, a more detailed characterization of transition state is required. In this work, we employ the interatomic distances and bond angles as input variables for deep learning, rather than the conventional and more elaborate dihedral angles. Our approach utilizes deep learning to investigate whether changes in the main chain dihedral angle can be expressed in terms of interatomic distances and bond angles. Furthermore, by incorporating XAI into our predictive analysis, we quantified the importance of each input variable and succeeded in clarifying the specific interatomic distance that affects the transition state. The results indicate that constructing a free energy landscape based on using the identified interatomic distance can clearly distinguish between the two stable states and provide a comprehensive explanation for the energy barrier crossing.

I. INTRODUCTION

In various complex molecular systems, such as protein conformational changes, the central task often involves the selection of one or two collective variables (CVs) to characterize the free energy landscape (FEL). Specifically, the probability distribution function $P(r)$ for a chosen CV r from a large number of CV candidates is obtained through molecular dynamics (MD) simulations. By taking its logarithmic form, $F(r) = -k_{\text{B}}T \ln P(r)$ serves as the representation of the FEL.¹ Within the FEL, if stable states are distinguished by a saddle point, and moreover the transition pathway passes through the saddle point on the FEL, the variable r is regarded as the reaction coordinate (RC) governing the target change.² In this context, the saddle point of the FEL can be regarded as the transition state (TS).

The isomerization of alanine dipeptide serves as a model for dihedral angle changes in proteins and represents a benchmark in exploring the complexities of FEL (see Fig. 1(a)). Conventionally, the FEL of the alanine dipeptide isomerization has been described as a function of two key dihedral angles, φ (C-N-C $_{\alpha}$ -C) and ψ (N-C $_{\alpha}$ -C-N), often referred to as

the Ramachandran plot.³ In vacuum, two stable states, $C7_{\text{eq}}$ (β -sheet structure) and $C7_{\text{ax}}$ (left handed α -helix structure), are well characterized by the FEL using φ and ψ . Hereafter, $C7_{\text{eq}}$ and $C7_{\text{ax}}$ are denoted as states A and B, respectively (see Fig. 1(b)).

The transition path sampling and committor analysis, when applied to the alanine dipeptide in vacuum, have unveiled the necessity of incorporating another dihedral angle, θ (O-C-N-C $_{\alpha}$), to adequately describe the FEL for the conformational change between the two states A and B.⁴ Here, the committor, denoted as $p_{\text{B}}^*(\mathbf{x})$, represents the probability of the trajectories reaching state B before state A starting from the initial configuration \mathbf{x} produced by the Maxwell–Boltzmann velocity distribution at temperature T .^{5–16} The selected CVs used to describe the FEL can be considered the primary contributors to the RC if the distribution of evaluated committor $p_{\text{B}}^*(\mathbf{x})$ of varieties of configurations \mathbf{x} continuously changes from 0 to 1.^{17–40} Correspondingly, the TS is characterized by the collection of configurations \mathbf{x} exhibiting $p_{\text{B}}^* = 0.5$.

Machine learning stands out as one of the most promising methods for automatically identifying the appropriate CVs relevant to RC.^{41–65} The pioneering work by Ma and Dinner introduced an automated search approach for identifying adequate CVs in alanine dipeptide isomerization using a genetic algorithm.⁶⁶ Expanding on this, we have utilized alternative machine learning techniques such as linear regression and deep neural networks, considering all possible dihedral angles of alanine dipeptide as candidate CVs.^{67,68} Significantly, our

^{a)}Electronic mail: keokazaki@ims.ac.jp

^{b)}Electronic mail: toshi_mori@cm.kyushu-u.ac.jp

^{c)}Electronic mail: kk@cheng.es.osaka-u.ac.jp

^{d)}Electronic mail: nobuyuki@cheng.es.osaka-u.ac.jp

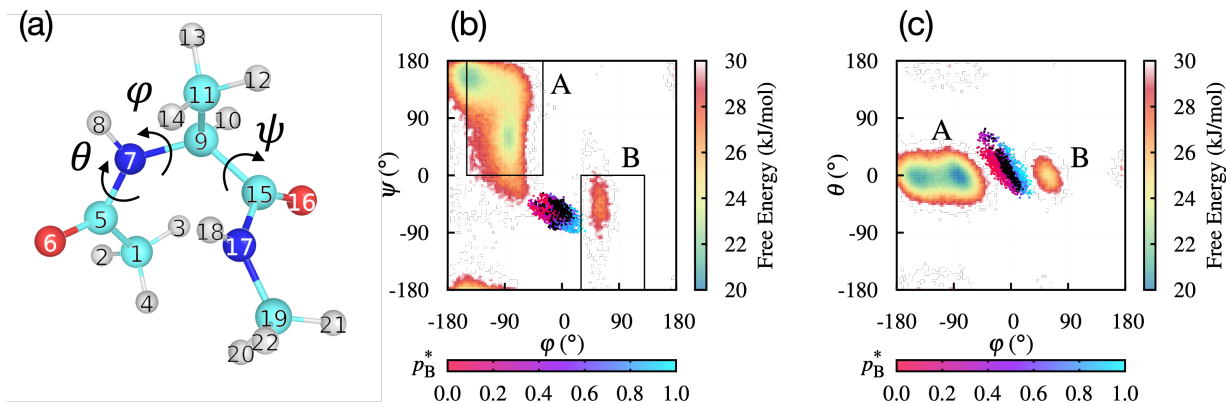


FIG. 1. (a) Index assigned to alanine dipeptide atoms. Major three dihedral angles φ , ψ , and θ are also described. (b) and (c): Two-dimensional FELs using (φ, ψ) (b) and (φ, θ) (c). In (b), the black boxes describe states A $[(-150^\circ, 0^\circ) \leq (\varphi, \psi) \leq (-30^\circ, 180^\circ)]$ and B $[(30^\circ, -180^\circ) \leq (\varphi, \psi) \leq (130^\circ, 0^\circ)]$. The points represents sampled 1,000 shooting points (training data set), which are colored by p_B^* values given in the bottom color bar. Note that the total number of shooting points is 2000 and that 1000 of them are shown in (b) and (c) as the training dataset. In addition, the points with $p_B^* \sim 0.5$ ($0.45 \leq p_B^* \leq 0.55$) are marked in black dots.

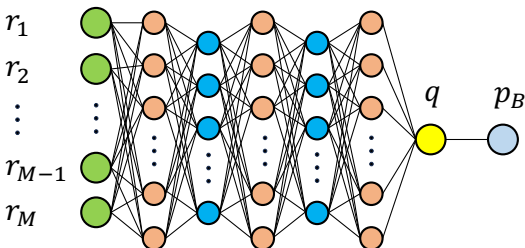


FIG. 2. Schematic diagram of the neural network architecture for the training of the relationship between committor value p_B^* and M CVs plus 1 bias term $\mathbf{r} = (1, r_1, r_2, \dots, r_M)$, and predicting committor p_B as a sigmoidal committor function $p_B(q) = (1 + \tanh(q))/2$. The neural network involves five hidden layers, of which the odd- and even-numbered layers had 400 and 200 nodes, respectively. Note that the node representing the bias term is omitted from the diagram.

investigation highlighted the effectiveness of the ‘‘Explainable AI (XAI)’’ method in providing a local explanation model for the data along the RC. As a result, the description of the separatrix line on the FEL has been suitably characterized by $p_B^* = 0.5$, employing two dihedral angles φ and θ (see Fig. 1(c)).⁶⁸ Recently, sophisticated methodologies, such as persistent homology⁶⁹ and Light Gradient Boosting Machine (LightGBM),⁷⁰ have been utilized in transition path samplings for the isomerization of alanine dipeptide.

It is of significance to emphasize that the scope of CVs extends beyond dihedral angles to include interatomic distances and bond angles, all of which represent plausible candidates for describing the FEL. Dihedral angles, derived from four adjacent atoms, play a crucial role in elucidating protein conformations, while interatomic distances and bond angles, being variables of relatively simpler computation, provide a more general means of analysis compared to dihedral angles. Hence, in this study, we employ interatomic distances and bond angles of alanine dipeptide as input variables for the

neural network. Furthermore, the application of XAI facilitates a comprehensive understanding of CVs that influence the RC, without relying solely on dihedral angles.

II. METHODS

A. Simulation details

We conducted a numerical examination of the alanine dipeptide isomerization in vacuum using MD simulations. The system consists of a single alanine dipeptide molecule, and the MD procedures are described in Refs. 67 and 68. Configurations of the alanine dipeptide were collected through a transition path sampling technique known as aimless shooting.¹² In this method, trajectories are produced with distinctly sampled momenta from the Maxwell–Boltzmann distribution at 300 K for each configuration. Specifically, the aimless shooting was initiated from a configuration randomly chosen from the region between the two states, A and B, as described in Fig. 1(b). A total of 2,000 shooting points were sampled. Furthermore, for each shooting point, we determined the committor p_B^* by running 1 ps MD simulations 100 times, employing random velocities from the Maxwell–Boltzmann distribution at 300 K (additional numerical conditions can be found in Ref. 67). We also computed all 45 dihedral angles (including 4 improper dihedral angles), 210 interatomic distances, and 36 bond angles within the molecule as CV candidates for each configuration. See Tables S1-S3 of the supplementary material for detailed definitions of the dihedral angles, interatomic distances, and bond angles. For describing FELs in this study, the replica-exchange MD simulations were employed, the detail of which is also available in Ref. 67.

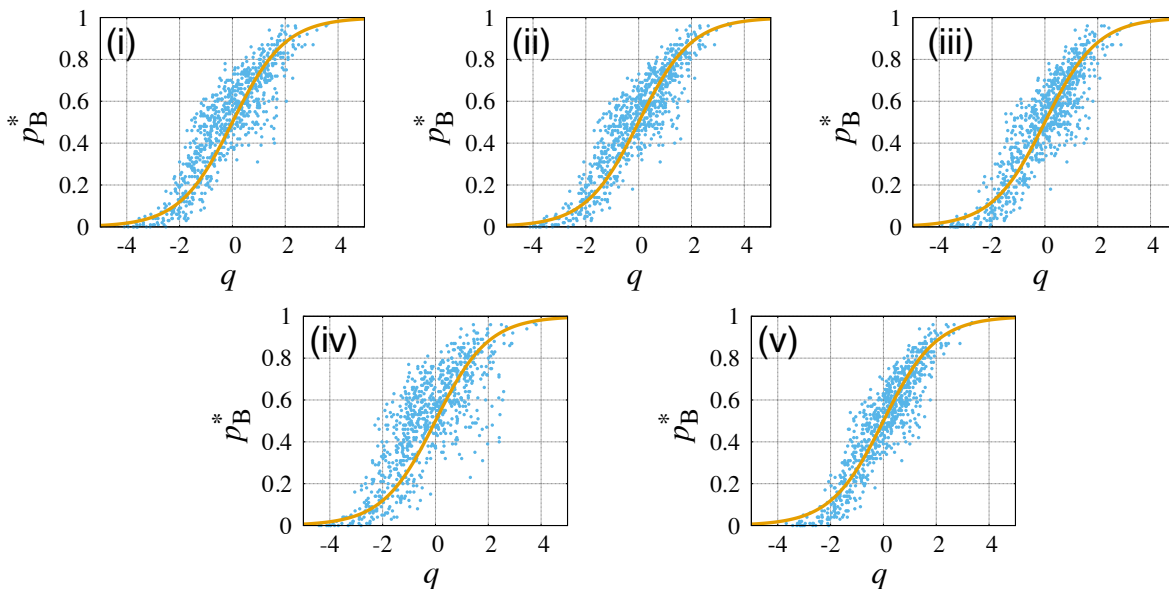


FIG. 3. Relationship between p_B^* and q derived from the neural network trained model using test dataset (800 points). The orange curve represents the sigmoidal function $p_B(q) = (1 + \tanh(q))/2$. Input variables for each case are as follows: (i) 90 dihedral angles, 210 interatomic distances, and 36 bond angles, (ii) 90 dihedral angles and 210 interatomic distances, (iii) 210 interatomic distances and 36 bond angles, (iv) 90 dihedral angles and 36 bond angles, and (v) 210 interatomic distances.

B. Neural network learning and XAI

We employed neural network learning to predict the relationship between the committor distribution p_B^* and candidate CVs. The architecture of the neural network is identical to that utilized in our previous study, as described in Fig. 2.⁶⁸ Bond angles are presented in the cosine form, while dihedral angles are transformed into both cosine and sine forms, resulting in a total of 90 CVs. All CVs, including dihedral angles, interatomic distances, and bond angles, were standardized.

We utilized various combinations of input variable types for the neural networks: (i) 90 dihedral angles, 210 interatomic distances, and 36 bond angles, (ii) 90 dihedral angles and 210 interatomic distances, (iii) 210 interatomic distances and 36 bond angles, (iv) 90 dihedral angles and 36 bond angles, and (v) 210 interatomic distances. Correspondingly, the total number of input variables M is (i) $M = 336$, (ii) $M = 300$, (iii) $M = 246$, (iv) $M = 126$, and (v) $M = 210$, respectively. Through the network with five hidden layers, where the odd- and even-numbered layers consist of 400 and 200 nodes each, respectively, a one-dimensional variable q is derived. The neural network is trained to ensure the regression of the relationship between q and p_B^* to a sigmoidal function, represented as $p_B(q) = (1 + \tanh(q))/2$, where q serves as the RC. The dataset of CVs and committor values from 2,000 configurations was partitioned into training, validation, and test datasets at a ratio of 5:1:4. (additional numerical conditions are described in Ref. 68). Note that we attempted to train the same neural network with 36 bond angle as input variables. However, the obtained training results were insufficient, and we decided not to include them in this paper. In fact, the distribution of any bond angles fluctuates around the

mean value and is unsuitable for distinguishing between the two stable states, A and B.

For elucidating the deep learning model, we employed two types of XAI method, Local Interpretable Model-agnostic Explanation (LIME)⁷¹ and Shapley Additive exPlanations (SHAP).⁷² Both methodologies are designed to quantify the importance of features in deep learning predictions and provide explanation models. LIME provides a linear regression model, elucidating the local behavior of a target instance explained by the perturbation of input variables with the Gauss kernel function. Note that LIME ignores the correlation among the features, causing the characteristics which may differ from the original dataset. In contrast, SHAP employs an additive feature attribution method, ensuring a fair distribution of predictions among input features in accordance with the game-theory-based Shapley value. Specifically, we utilized the Kernel SHAP, which calculates the Shapley value based on the LIME framework. Therefore, SHAP is expected to quantify the contribution of each feature more accurately than LIME.

In a previous work, we demonstrated the efficacy of XAI to identify the important features for the transition through the TS.⁶⁸ More precisely, the relevant CVs contributing to the RC q were identified as φ and θ , in contrast to φ and ψ . Note that an alternative application of SHAP to a deep learning using LightGBM in the alanine dipeptide isomerization has recently been reported.⁷⁰ In the current study, using LIME and SHAP, we quantified the contribution of input variables to the RC q for the five different results from deep learning, achieved by changing the combinations of CV types, *i.e.*, dihedral angle, interatomic distance, and bond angle.

TABLE I. Top five dominant contributions and those absolute values obtained using LIME and SHAP for various combinations of input variable types. The dihedral angles defined from atom numbers (X-5-7-Y) and (X-7-9-Y) denote θ and φ , respectively, with arbitrary atoms X and Y. The symbol * represents sine form of the improper dihedral angle defined by atom numbers (1-7-5-6).

| input variables | LIME | | | | SHAP | | | |
|-----------------------------------------------------------|----------------|-------|----------------|-------|----------------|-------|----------------|-------|
| | type | index | feature | value | type | index | feature | value |
| (i) dihedral angles + interatomic distances + bond angles | distance | 93 | r_{6-10} | 0.942 | distance | 95 | r_{6-12} | 0.026 |
| | distance | 95 | r_{6-12} | 0.920 | distance | 94 | r_{6-11} | 0.026 |
| | distance | 101 | r_{6-18} | 0.811 | distance | 93 | r_{6-10} | 0.023 |
| | distance | 100 | r_{6-17} | 0.683 | dihedral angle | 87 | * | 0.020 |
| | distance | 99 | r_{6-16} | 0.667 | distance | 101 | r_{6-18} | 0.015 |
| (ii) dihedral angles + interatomic distances | distance | 93 | r_{6-10} | 0.948 | distance | 93 | r_{6-10} | 0.033 |
| | distance | 95 | r_{6-12} | 0.928 | distance | 95 | r_{6-12} | 0.024 |
| | distance | 94 | r_{6-11} | 0.769 | distance | 94 | r_{6-11} | 0.020 |
| | distance | 100 | r_{6-17} | 0.721 | dihedral angle | 57 | $\sin \varphi$ | 0.019 |
| | dihedral angle | 58 | $\sin \varphi$ | 0.704 | distance | 100 | r_{6-17} | 0.019 |
| (iii) interatomic distances + bond angles | distance | 93 | r_{6-10} | 1.691 | distance | 93 | r_{6-10} | 0.039 |
| | distance | 95 | r_{6-12} | 1.440 | distance | 95 | r_{6-12} | 0.036 |
| | distance | 94 | r_{6-11} | 1.100 | distance | 94 | r_{6-11} | 0.032 |
| | distance | 100 | r_{6-17} | 1.034 | distance | 99 | r_{6-16} | 0.021 |
| | distance | 97 | r_{6-14} | 0.801 | distance | 100 | r_{6-17} | 0.017 |
| (iv) diheral angles + bond angles | dihedral angle | 55 | $\sin \theta$ | 2.514 | dihedral angle | 53 | $\sin \theta$ | 0.075 |
| | dihedral angle | 57 | $\sin \varphi$ | 1.921 | dihedral angle | 55 | $\sin \theta$ | 0.074 |
| | dihedral angle | 58 | $\sin \varphi$ | 1.636 | dihedral angle | 57 | $\sin \varphi$ | 0.056 |
| | dihedral angle | 56 | $\sin \varphi$ | 1.304 | dihedral angle | 11 | $\cos \varphi$ | 0.047 |
| | dihedral angle | 87 | * | 0.762 | dihedral angle | 58 | $\sin \varphi$ | 0.046 |
| (v) interactomic distances | distance | 93 | r_{6-10} | 1.609 | distance | 93 | r_{6-10} | 0.075 |
| | distance | 95 | r_{6-12} | 1.553 | distance | 94 | r_{6-11} | 0.074 |
| | distance | 94 | r_{6-11} | 1.248 | distance | 99 | r_{6-16} | 0.056 |
| | distance | 100 | r_{6-17} | 0.972 | distance | 95 | r_{6-12} | 0.047 |
| | distance | 101 | r_{6-18} | 0.950 | distance | 101 | r_{6-18} | 0.046 |

III. RESULTS AND DISCUSSION

A. Learning of committor p_B^* and RC q

Figure 3 shows the test data (800 points) results depicting the relationship between p_B^* and q derived from the training of the neural networks. Two different model evaluation metrics were employed: the coefficient of determination, R^2 , and the root mean square error, RMSE. Both metrics assess the fit of outcomes q to the sigmoidal function $p_B(q) = (1 + \tanh(q))/2$. The results for each case are as follows: (R^2 , RMSE) = (0.880, 0.130) (i), (0.899, 0.118) (ii), (0.885, 0.117) (iii), (0.889, 0.179) (iv), and (0.903, 0.103) (v). These results signify the overall success of p_B prediction through q . The inclusion of bond angles as input variables leads to a slight decrease in accuracy. As noted in Sec. II B, bonding angles prove insufficient for effectively distinguishing between the two states, contributing insignificantly to the outcomes of q .

B. CV contribution using LIME and SHAP

As detailed in Sec. II B, the influence of each input variable on the neural network prediction can be assessed through XAI methods, specifically LIME and Kernel SHAP. These methods elucidate the manner in which each feature contributes to the prediction using the additive feature attribution method.

We evaluated the feature contribution from all of the data (2000 points) using LIME and SHAP. The index dependence of the feature contribution in absolute value are illustrated in Fig. S1-S5 of the supplementary material for each input variable case. The comparison reveals that, for input variables with significant contributions, LIME and SHAP provide nearly consistent results. In contrast, for variables with smaller contributions, LIME tends to yield output values that are more suppressed compared to SHAP, particularly noticeable for indices 1-89 of interatomic distances. Interestingly, LIME assesses that interatomic distances involving atoms 1-5 are irrelevant to the target conformation change between the two stable states, A and B. This difference between LIME and SHAP can be attributed to the fact that LIME quantifies the contribution to prediction through linear regression, where the correlation among input features is not taken into account, as mentioned in Sec. II B.

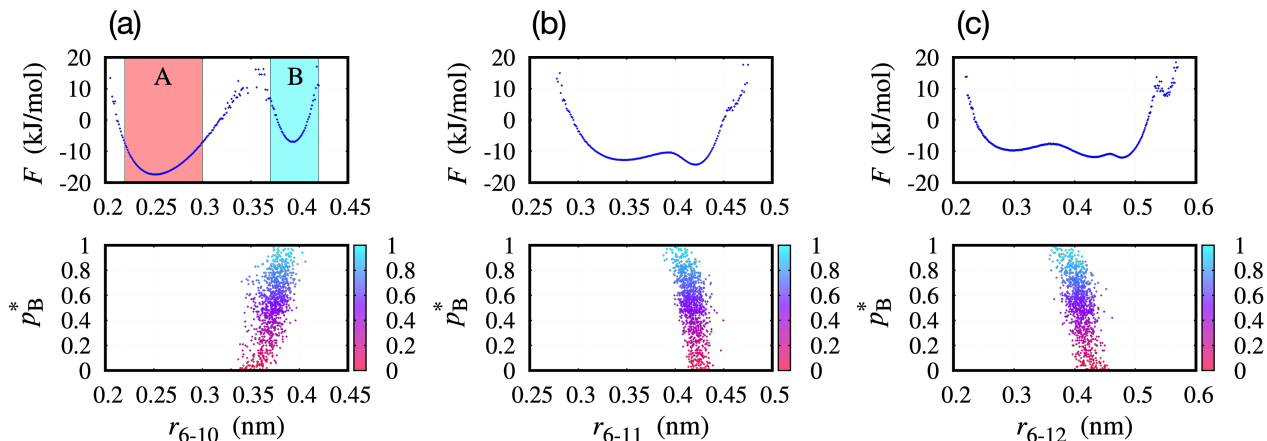


FIG. 4. (Top) FEL using CV, r_{6-10} (a), r_{6-11} (b), and r_{6-12} (c). In (a), the ranges of $0.22 \text{ nm} \leq r_{6-10} \leq 0.30 \text{ nm}$ and $0.37 \text{ nm} \leq r_{6-10} \leq 0.42 \text{ nm}$ effectively represent states A and B, respectively. (Bottom) Corresponding committor p_B^* distribution as a function of each CV.

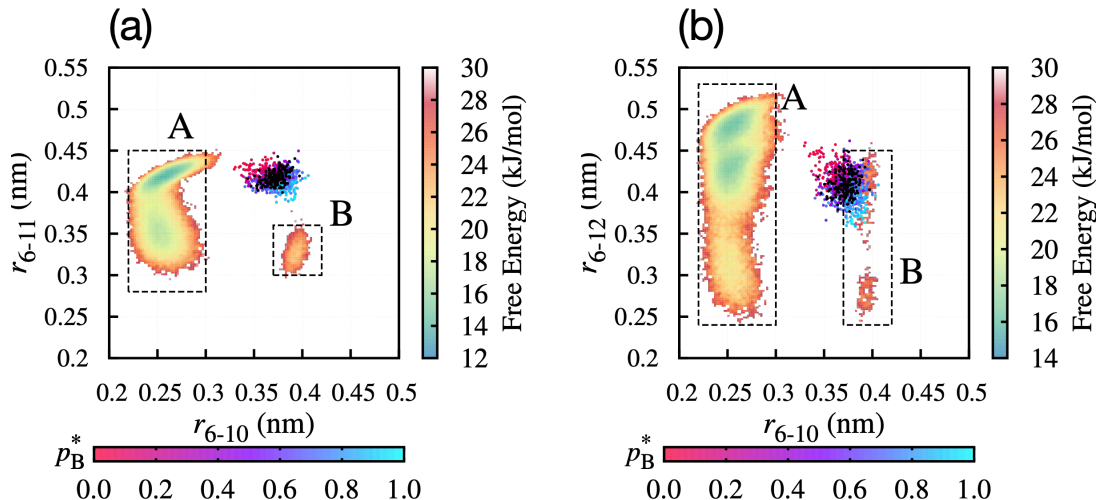


FIG. 5. Two-dimensional FELs using (r_{6-10}, r_{6-11}) (a) and (r_{6-10}, r_{6-12}) (b). The points represent sampled 1,000 shooting points (training data set), which are colored by p_B^* values given in the bottom color bar. The black boxes with dashed lines practically correspond to states A and B, characterized as $[(0.22 \text{ nm}, 0.28 \text{ nm}) \leq (r_{6-10}, r_{6-11}) \leq (0.30 \text{ nm}, 0.45 \text{ nm})]$ in (a) and $[(0.22 \text{ nm}, 0.24 \text{ nm}) \leq (r_{6-10}, r_{6-12}) \leq (0.30 \text{ nm}, 0.53 \text{ nm})]$ in (b), and $[(0.37 \text{ nm}, 0.30 \text{ nm}) \leq (r_{6-10}, r_{6-11}) \leq (0.42 \text{ nm}, 0.36 \text{ nm})]$ in (a) and $[(0.37 \text{ nm}, 0.27 \text{ nm}) \leq (r_{6-10}, r_{6-12}) \leq (0.42 \text{ nm}, 0.45 \text{ nm})]$ in (b), respectively. Note that these boundaries are different from those in Fig. 1(b), which are used in the aimless shooting. In addition, the points with $p_B^* \sim 0.5$ ($0.45 \leq p_B^* \leq 0.55$) are marked in black dots.

Table I presents the top five dominant contributions along with their absolute values for each input variable case. Remarkably, in cases (i), (ii), (iii), and (v), interatomic distances between atom 6 and atoms (10, 11, 12) occupy the top two positions in both LIME and SHAP analyses. As depicted in Fig. 1(a), these distances are related to the dominant two angles φ and θ , making substantial contributions to the RC, q . From an intuitive standpoint, one might expect the interatomic distance between atoms 6 and 18, r_{6-18} , to be significant, given the consideration of hydrogen-bond formation. However, our observations indicate that the extent of its importance is limited. In fact, the variations in r_{6-18} are connected to changes in the dihedral angle ψ , a factor found to have a minor role in the investigated isomerization process.⁴

In case (iv), using 90 dihedral angles and 36 bond angles, the dihedral angles θ and φ emerge as the most dominant features. This observation is consistent with a prior study that employed 90 dihedral angles as input variables.⁶⁸ However, the current results reveal an increased importance of θ relative to φ compared to the previous findings. This reversal can be attributed to the slight degradation in the learning performances associated with the inclusion of bond angles, as discussed in Sec. III A. This influence is presumed to impact the outcomes of LIME and SHAP analyses.

C. FELs using interatomic distances

The LIME and SHAP results consistently highlight that the interatomic distances r_{6-10} , r_{6-11} , and r_{6-12} might be the CVs that significantly contribute to the RC, q . Figure 4 illustrates the FEL and corresponding committor p_B^* distribution as a function of each CV, namely, r_{6-10} (a), r_{6-11} (b), and r_{6-12} (c). As evident in Fig. 4(a), the FEL using r_{6-10} reveals that the two stable states are distinguished by the free energy barrier. Furthermore, the position of the barrier, $r_{6-10}^* = 0.36$ nm, approximately corresponds to $p_B^* = 0.5$, representing the TS. States A and B are practically delineated by specific ranges of the interatomic distance r_{6-10} , namely $0.22 \text{ nm} \leq r_{6-10} \leq 0.30 \text{ nm}$ for state A and $0.37 \text{ nm} \leq r_{6-10} \leq 0.42 \text{ nm}$ for state B. Since states A and B are originally defined in the FEL using φ and ψ as depicted in Fig. 1(b), the above thresholds expressed with r_{6-10} may not exactly correspond to those defined by φ and ψ . In contrast, as depicted in Fig. 4(b) and (c), other CVs, r_{6-11} and r_{6-12} , exhibit less consistency in describing the FEL with the committor p_B^* distribution. In particular, the free energy barriers are not distinctly observed, suggesting that these variables alone are insufficient for describing the FEL.

Finally, it is of interest to explore the two-dimensional FEL using possible combinations of the identified dominant CVs, namely (r_{6-10}, r_{6-11}) and (r_{6-10}, r_{6-12}) , as illustrated in Fig. 5. The combination of (r_{6-11}, r_{6-12}) was excluded because the free energy barrier is insufficiently described using r_{6-11} and r_{6-12} , as observed in Fig. 4(b) and (c). Figure 5 illustrates the discrimination between the two states, A and B, manifested by the separatrix line composed of the data points with $p_B^* \sim 0.5$, indicative of the TS. Note that the regions corresponding to states A and B, as described in Fig. 5, may not precisely match those in Fig. 1(b). Mapping the rectangular region depicted in Fig. 1(b) using (r_{6-10}, r_{6-11}) and (r_{6-10}, r_{6-12}) would lead to a more complex boundary than a simple rectangle. As illustrated in Fig. 5(a), the two-dimensional FEL using r_{6-10} and r_{6-11} provides an alternative representation of FEL, complementing the FEL using φ and θ (see Fig. 1(c)). Notably, the separatrix line indicates the negative correlation between r_{6-10} and r_{6-11} , suggesting that the barrier crossing from state A to B requires an increase in r_{6-10} and a decrease in r_{6-11} . This behavior near the TS is consistent with the r_{6-10} and r_{6-11} dependence of the committor distribution, as observed in Fig. 4(a) and (b). A similar behavior near the TS is observed in the two-dimensional FEL using r_{6-10} and r_{6-12} (see Fig. 5(b)), although the separatrix line is not as clearly seen compared to Fig. 5(a). Furthermore, the region corresponding to state B appears divided into two, with some overlap with the TS region. These results suggest that r_{6-11} is a more suitable CV than r_{6-12} for describing the FEL alongside r_{6-10} .

IV. CONCLUSIONS

Conventionally, the FEL concerning the conformational change in alanine dipeptide has been effectively described using specific main chain dihedral angles. However, our investigation recognized the need for a more detailed characteri-

zation, through the incorporation of more fundamental CVs such as interatomic distances and bond angles, within the machine learning approach for the identifying RC. By integrating XAI methods, specifically LIME and SHAP, into the machine learning predictions, we assessed the importance of each input variable, and successfully elucidated the specific interatomic distance, dominantly r_{6-10} , in accord with the committor p_B^* distribution. The results manifest that constructing the FEL using the identified interatomic distance differentiates between the two stable states and clarifies the process of barrier crossing through the TS.

Furthermore, our investigation into the two-dimensional FEL using the two dominant interatomic distances, r_{6-10} and r_{6-11} , provided insights into the conformational changes between states A and B. Specifically, the separatrix line, described by data points with $p_B^* \sim 0.5$, was clearly observed as the indicator of the TS. This separatrix line aligns with the observations in the two-dimensional FEL using two major dihedral angles, φ and θ , emphasizing the importance of considering specific interatomic distances in capturing the target TS. Nonetheless, utilizing interatomic distance as input variables implies a reliance on pre-documented physical information. A potential future perspective involves utilizing graph neural networks to autonomously generate features based on the graph structure, thereby obtaining RC without relying on the physics-informed variables.

Deciding between LIME and SHAP, or consistently employing both, is an aspect worth considering. The SHAP, developed as an additive feature attribution method based on LIME, has the advantage of having a theoretical basis in game theory. Since the prediction results are distributed fairly among the features, it is expected that the contribution of each feature can be quantified more accurately than LIME. However, the computational cost of SHAP increases exponentially with the number of features because it is necessary to calculate the Shapley value for the number of combinations to be considered. Given that the machine learning model used in this study is a relatively simple regression on the sigmoidal function, which is a monotonically increasing function, the variables with large contributions identified by LIME and Kernel SHAP are considered to be consistent.

The optimization of hyperparameters for neural networks is another crucial aspect to consider. The selection of the numbers of hidden layers and nodes significantly impacts the generalization performance of the neural network, thereby influencing the results obtained through XAI analyses. Our ongoing efforts are dedicated to exploring and implementing optimizations in this direction.

SUPPLEMENTARY MATERIAL

The supplementary material include definitions of dihedral angles, interatomic distances, and bond angles (Tables S1-S3), and feature contribution of each input variable using LIME and SHAP for each input variable case (Figs. S1-S5).

ACKNOWLEDGMENTS

This work was supported by JSPS KAKENHI Grant-in-Aid Grant Nos. JP22H02595, JP22H02035, JP22H04542, JP22K03550, JP23H02622, JP23K23303, JP23K23858, JP23K27313, and JP24H01719. We acknowledge supports from the Fugaku Supercomputing Project (Nos. JPMXP1020230325 and JPMXP1020230327) and the Data-Driven Material Research Project (No. JPMXP1122714694) from the Ministry of Education, Culture, Sports, Science, and Technology. The numerical calculations were performed at Research Center for Computational Science, Okazaki Research Facilities, National Institutes of Natural Sciences (Projects: 24-IMS-C051 and 24-IMS-C198) and at the Cybermedia Center, Osaka University.

- ¹D. M. Zuckerman, *Statistical Physics of Biomolecules: An Introduction* (CRC press, Boca Raton, FL, 2010).
- ²B. Peters, *Reaction Rate Theory and Rare Events* (Elsevier, Amsterdam, 2017).
- ³G. N. Ramachandran and V. Sasisekharan, "Conformation of Polypeptides and Proteins," in *Advances in Protein Chemistry*, Vol. 23, edited by C. B. Anfinsen, M. L. Anson, J. T. Edsall, and F. M. Richards (1968) pp. 283–437.
- ⁴P. G. Bolhuis, C. Dellago, and D. Chandler, "Reaction coordinates of biomolecular isomerization," *Proc. Natl. Acad. Sci. U.S.A.* **97**, 5877–5882 (2000).
- ⁵R. Du, V. S. Pande, A. Y. Grosberg, T. Tanaka, and E. S. Shakhnovich, "On the transition coordinate for protein folding," *J. Chem. Phys.* **108**, 334–350 (1998).
- ⁶P. L. Geissler, C. Dellago, and D. Chandler, "Kinetic Pathways of Ion Pair Dissociation in Water," *J. Phys. Chem. B* **103**, 3706–3710 (1999).
- ⁷P. G. Bolhuis, D. Chandler, C. Dellago, and P. L. Geissler, "Transition Path Sampling: Throwing Ropes Over Rough Mountain Passes, in the Dark," *Annu. Rev. Phys. Chem.* **53**, 291–318 (2002).
- ⁸G. Hummer, "From transition paths to transition states and rate coefficients," *J. Chem. Phys.* **120**, 516–523 (2004).
- ⁹R. B. Best and G. Hummer, "Reaction coordinates and rates from transition paths," *Proc. Natl. Acad. Sci. U.S.A.* **102**, 6732–6737 (2005).
- ¹⁰W. E, W. Ren, and E. Vanden-Eijnden, "Transition pathways in complex systems: Reaction coordinates, isocommittor surfaces, and transition tubes," *Chem. Phys. Lett.* **413**, 242–247 (2005).
- ¹¹B. Peters, "Using the histogram test to quantify reaction coordinate error," *J. Chem. Phys.* **125**, 241101 (2006).
- ¹²B. Peters and B. L. Trout, "Obtaining reaction coordinates by likelihood maximization," *J. Chem. Phys.* **125**, 054108 (2006).
- ¹³B. Peters, G. T. Beckham, and B. L. Trout, "Extensions to the likelihood maximization approach for finding reaction coordinates," *J. Chem. Phys.* **127**, 034109 (2007).
- ¹⁴B. Peters, "P(TP) $_{\eta}$ peak maximization: Necessary but not sufficient for reaction coordinate accuracy," *Chem. Phys. Lett.* **494**, 100–103 (2010).
- ¹⁵B. Peters, "Reaction Coordinates and Mechanistic Hypothesis Tests," *Annu. Rev. Phys. Chem.* **67**, 669–690 (2016).
- ¹⁶H. Jung, K.-i. Okazaki, and G. Hummer, "Transition path sampling of rare events by shooting from the top," *J. Chem. Phys.* **147**, 152716 (2017).
- ¹⁷M. F. Hagan, A. R. Dinner, D. Chandler, and A. K. Chakraborty, "Atomistic understanding of kinetic pathways for single base-pair binding and unbinding in DNA," *Proc. Natl. Acad. Sci. U.S.A.* **100**, 13922–13927 (2003).
- ¹⁸A. C. Pan and D. Chandler, "Dynamics of Nucleation in the Ising Model," *J. Phys. Chem. B* **108**, 19681–19686 (2004).
- ¹⁹Y. M. Rhee and V. S. Pande, "One-Dimensional Reaction Coordinate and the Corresponding Potential of Mean Force from Commitment Probability Distribution," *J. Phys. Chem. B* **109**, 6780–6786 (2005).
- ²⁰A. Berezhkovskii and A. Szabo, "One-dimensional reaction coordinates for diffusive activated rate processes in many dimensions," *J. Chem. Phys.* **122**, 014503 (2005).
- ²¹D. Moroni, P. R. ten Wolde, and P. G. Bolhuis, "Interplay between Structure and Size in a Critical Crystal Nucleus," *Phys. Rev. Lett.* **94**, 235703 (2005).
- ²²D. Branduardi, F. L. Gervasio, and M. Parrinello, "From A to B in free energy space," *J. Chem. Phys.* **126**, 054103 (2007).
- ²³S. L. Quaytman and S. D. Schwartz, "Reaction coordinate of an enzymatic reaction revealed by transition path sampling," *Proc. Natl. Acad. Sci. U.S.A.* **104**, 12253–12258 (2007).
- ²⁴G. T. Beckham, B. Peters, C. Starbuck, N. Variankaval, and B. L. Trout, "Surface-Mediated Nucleation in the Solid-State Polymorph Transformation of Terephthalic Acid," *J. Am. Chem. Soc.* **129**, 4714–4723 (2007).
- ²⁵B. Peters, N. E. R. Zimmermann, G. T. Beckham, J. W. Tester, and B. L. Trout, "Path Sampling Calculation of Methane Diffusivity in Natural Gas Hydrates from a Water-Vacancy Assisted Mechanism," *J. Am. Chem. Soc.* **130**, 17342–17350 (2008).
- ²⁶G. T. Beckham, B. Peters, and B. L. Trout, "Evidence for a Size Dependent Nucleation Mechanism in Solid State Polymorph Transformations," *J. Phys. Chem. B* **112**, 7460–7466 (2008).
- ²⁷D. Antoniou and S. D. Schwartz, "The stochastic separatrix and the reaction coordinate for complex systems," *J. Chem. Phys.* **130**, 151103 (2009).
- ²⁸L. Xi, M. Shah, and B. L. Trout, "Hopping of Water in a Glassy Polymer Studied via Transition Path Sampling and Likelihood Maximization," *J. Phys. Chem. B* **117**, 3634–3647 (2013).
- ²⁹S. Jungblut, A. Singraber, and C. Dellago, "Optimising reaction coordinates for crystallisation by tuning the crystallinity definition," *Mol. Phys.* **111**, 3527–3533 (2013).
- ³⁰B. C. Barnes, B. C. Knott, G. T. Beckham, D. T. Wu, and A. K. Sum, "Reaction Coordinate of Incipient Methane Clathrate Hydrate Nucleation," *J. Phys. Chem. B* **118**, 13236–13243 (2014).
- ³¹R. G. Mullen, J.-E. Shea, and B. Peters, "Transmission Coefficients, Committers, and Solvent Coordinates in Ion-Pair Dissociation," *J. Chem. Theory Comput.* **10**, 659–667 (2014).
- ³²R. G. Mullen, J.-E. Shea, and B. Peters, "Easy Transition Path Sampling Methods: Flexible-Length Aimless Shooting and Permutation Shooting," *J. Chem. Theory Comput.* **11**, 2421–2428 (2015).
- ³³L. Lupi, B. Peters, and V. Molinero, "Pre-ordering of interfacial water in the pathway of heterogeneous ice nucleation does not lead to a two-step crystallization mechanism," *J. Chem. Phys.* **145**, 211910 (2016).
- ³⁴M. Ernst, S. Wolf, and G. Stock, "Identification and Validation of Reaction Coordinates Describing Protein Functional Motion: Hierarchical Dynamics of T4 Lysozyme," *J. Chem. Theory Comput.* **13**, 5076–5088 (2017).
- ³⁵G. Díaz Leines and J. Rogal, "Maximum Likelihood Analysis of Reaction Coordinates during Solidification in Ni," *J. Phys. Chem. B* **122**, 10934–10942 (2018).
- ³⁶M. N. Joswiak, M. F. Doherty, and B. Peters, "Ion dissolution mechanism and kinetics at kink sites on NaCl surfaces," *Proc. Natl. Acad. Sci. U.S.A.* **115**, 656–661 (2018).
- ³⁷K.-i. Okazaki, D. Wöhlert, J. Warnau, H. Jung, Ö. Yildiz, W. Kühlbrandt, and G. Hummer, "Mechanism of the electroneutral sodium/proton antiporter PanHaP from transition-path shooting," *Nat. Commun.* **10**, 1742 (2019).
- ³⁸T. Mori and S. Saito, "Dissecting the Dynamics during Enzyme Catalysis: A Case Study of Pin1 Peptidyl-Prolyl Isomerase," *J. Chem. Theory Comput.* **16**, 3396–3407 (2020).
- ³⁹N. Schwier, "Kinetic pathways of water exchange in the first hydration shell of magnesium," *J. Chem. Phys.* **152**, 224106 (2020).
- ⁴⁰R. L. Silveira, B. C. Knott, C. S. Pereira, M. F. Crowley, M. S. Skaf, and G. T. Beckham, "Transition Path Sampling Study of the Feruloyl Esterase Mechanism," *J. Phys. Chem. B* **125**, 2018–2030 (2021).
- ⁴¹F. Sittel and G. Stock, "Robust Density-Based Clustering To Identify Metastable Conformational States of Proteins," *J. Chem. Theory Comput.* **12**, 2426–2435 (2016).
- ⁴²M. M. Sultan and V. S. Pande, "Automated design of collective variables using supervised machine learning," *J. Chem. Phys.* **149**, 094106 (2018).
- ⁴³C. Wehmeyer and F. Noé, "Time-lagged autoencoders: Deep learning of slow collective variables for molecular kinetics," *J. Chem. Phys.* **148**, 241703 (2018).
- ⁴⁴A. Mardt, L. Pasquali, H. Wu, and F. Noé, "VAMPnets for deep learning of molecular kinetics," *Nat. Commun.* **9**, 5 (2018).
- ⁴⁵A. Bittracher, R. Banisch, and C. Schütte, "Data-driven computation of molecular reaction coordinates," *J. Chem. Phys.* **149**, 154103 (2018).

- ⁴⁶W. Chen and A. L. Ferguson, “Molecular enhanced sampling with autoencoders: On-the-fly collective variable discovery and accelerated free energy landscape exploration,” *J. Comput. Chem.* **39**, 2079–2102 (2018).
- ⁴⁷J. M. L. Ribeiro, P. Bravo, Y. Wang, and P. Tiwary, “Reweighted autoencoded variational Bayes for enhanced sampling (RAVE),” *J. Chem. Phys.* **149**, 072301 (2018).
- ⁴⁸J. Rogal, E. Schneider, and M. E. Tuckerman, “Neural-Network-Based Path Collective Variables for Enhanced Sampling of Phase Transformations,” *Phys. Rev. Lett.* **123**, 245701 (2019).
- ⁴⁹Y. Wang, J. M. Lamim Ribeiro, and P. Tiwary, “Machine learning approaches for analyzing and enhancing molecular dynamics simulations,” *Curr. Opin. Struct. Biol.* **61**, 139–145 (2020).
- ⁵⁰L. Bonati, V. Rizzi, and M. Parrinello, “Data-Driven Collective Variables for Enhanced Sampling,” *J. Phys. Chem. Lett.* **11**, 2998–3004 (2020).
- ⁵¹H. Sidky, W. Chen, and A. L. Ferguson, “Machine learning for collective variable discovery and enhanced sampling in biomolecular simulation,” *Mol. Phys.* **118**, e1737742 (2020).
- ⁵²D. Wang and P. Tiwary, “State predictive information bottleneck,” *J. Chem. Phys.* **154**, 134111 (2021).
- ⁵³J. Zhang, Y.-K. Lei, Z. Zhang, X. Han, M. Li, L. Yang, Y. I. Yang, and Y. Q. Gao, “Deep reinforcement learning of transition states,” *Phys. Chem. Chem. Phys.* **23**, 6888–6895 (2021).
- ⁵⁴M. Frassek, A. Arjun, and P. G. Bolhuis, “An extended autoencoder model for reaction coordinate discovery in rare event molecular dynamics datasets,” *J. Chem. Phys.* **155**, 064103 (2021).
- ⁵⁵F. Hoofit, A. Pérez de Alba Ortíz, and B. Ensing, “Discovering Collective Variables of Molecular Transitions via Genetic Algorithms and Neural Networks,” *J. Chem. Theory Comput.* **17**, 2294–2306 (2021).
- ⁵⁶L. Bonati, G. Piccini, and M. Parrinello, “Deep learning the slow modes for rare events sampling,” *Proc. Natl. Acad. Sci. U.S.A.* **118**, e2113533118 (2021).
- ⁵⁷M. Chen, “Collective variable-based enhanced sampling and machine learning,” *Eur. Phys. J. B* **94**, 211 (2021).
- ⁵⁸Z. Belkacemi, P. Gkeka, T. Lelièvre, and G. Stoltz, “Chasing Collective Variables Using Autoencoders and Biased Trajectories,” *J. Chem. Theory Comput.* **18**, 59–78 (2022).
- ⁵⁹J. Neumann and N. Schwierz, “Artificial Intelligence Resolves Kinetic Pathways of Magnesium Binding to RNA,” *J. Chem. Theory Comput.* **18**, 1202–1212 (2022).
- ⁶⁰D. Ray, E. Trizio, and M. Parrinello, “Deep learning collective variables from transition path ensemble,” *J. Chem. Phys.* **158**, 204102 (2023).
- ⁶¹H. Jung, R. Covino, A. Arjun, C. Leitold, C. Dellago, P. G. Bolhuis, and G. Hummer, “Machine-guided path sampling to discover mechanisms of molecular self-organization,” *Nat. Comput. Sci.* **3**, 334–345 (2023).
- ⁶²L. Bonati, E. Trizio, A. Rizzi, and M. Parrinello, “A unified framework for machine learning collective variables for enhanced sampling simulations: Micolvar,” *J. Chem. Phys.* **159**, 014801 (2023).
- ⁶³A. N. Singh and D. T. Limmer, “Variational deep learning of equilibrium transition path ensembles,” *J. Chem. Phys.* **159**, 024124 (2023).
- ⁶⁴S. Liang, A. N. Singh, Y. Zhu, D. T. Limmer, and C. Yang, “Probing reaction channels via reinforcement learning,” *Mach. Learn.: Sci. Technol.* **4**, 045003 (2023).
- ⁶⁵G. Lazzeri, H. Jung, P. G. Bolhuis, and R. Covino, “Molecular Free Energies, Rates, and Mechanisms from Data-Efficient Path Sampling Simulations,” *J. Chem. Theory Comput.* **19**, 9060–9076 (2023).
- ⁶⁶A. Ma and A. R. Dinner, “Automatic Method for Identifying Reaction Coordinates in Complex Systems,” *J. Phys. Chem. B* **109**, 6769–6779 (2005).
- ⁶⁷Y. Mori, K.-i. Okazaki, T. Mori, K. Kim, and N. Matubayasi, “Learning reaction coordinates via cross-entropy minimization: Application to alanine dipeptide,” *J. Chem. Phys.* **153**, 054115 (2020).
- ⁶⁸T. Kikutsuji, Y. Mori, K.-i. Okazaki, T. Mori, K. Kim, and N. Matubayasi, “Explaining reaction coordinates of alanine dipeptide isomerization obtained from deep neural networks using Explainable Artificial Intelligence (XAI),” *J. Chem. Phys.* **156**, 154108 (2022).
- ⁶⁹F. Manuchehrfar, H. Li, W. Tian, A. Ma, and J. Liang, “Exact Topology of the Dynamic Probability Surface of an Activated Process by Persistent Homology,” *J. Phys. Chem. B* **125**, 4667–4680 (2021).
- ⁷⁰N. Naleem, C. R. A. Abreu, K. Warmuz, M. Tong, S. Kirmizialtin, and M. E. Tuckerman, “An exploration of machine learning models for the determination of reaction coordinates associated with conformational transitions,” *J. Chem. Phys.* **159**, 034102 (2023).
- ⁷¹M. T. Ribeiro, S. Singh, and C. Guestrin, “‘‘Why Should I Trust You?’’: Explaining the Predictions of Any Classifier,” in *Proceedings of the 22nd ACM SIGKDD International Conference on Knowledge Discovery and Data Mining* (Association for Computing Machinery, San Francisco California, U.S.A., 2016) pp. 1135–1144.
- ⁷²S. M. Lundberg and S.-I. Lee, “A unified approach to interpreting model predictions,” in *Proceedings of the 31st international conference on neural information processing systems* (Curran Associates Inc., Red Hook, NY, 2017) pp. 4768–4777.

AUTHOR DECLARATIONS

CONFLICT OF INTEREST

The authors have no conflicts to disclose.

DATA AVAILABILITY STATEMENT

The data that support the findings of this study are available from the corresponding author upon reasonable request.

Supplementary Material

Unveiling interatomic distances influencing the reaction coordinates in alanine dipeptide isomerization: An explainable deep learning approach

Kazushi Okada,¹ Takuma Kikutsuji,¹ Kei-ichi Okazaki,^{2,3} Toshifumi Mori,^{4,5} Kang Kim,¹ and Nobuyuki Matubayasi¹

¹*Division of Chemical Engineering, Graduate School of Engineering Science, Osaka University, Osaka 560-8531, Japan*

²*Research Center for Computational Science, Institute for Molecular Science, Okazaki, Aichi 444-8585, Japan*

³*The Graduate University for Advanced Studies, Okazaki, Aichi 444-8585, Japan*

⁴*Institute for Materials Chemistry and Engineering, Kyushu University, Kasuga, Fukuoka 816-8580, Japan*

⁵*Interdisciplinary Graduate School of Engineering Sciences, Kyushu University, Kasuga, Fukuoka 816-8580, Japan*

TABLE S1. Definition of the dihedral angle index. The atom index is represented in Fig. 1(a). Note that dihedral angles are used in cosine (index: 1-45) and sine (index: 46-90) forms.

| index | index of atoms for dihedral angles | | |
|-------|------------------------------------|-------------------|-------------------|
| 1-3 | 2 - 1 - 5 - 6 | 2 - 1 - 5 - 7 | 3 - 1 - 5 - 6 |
| 4-6 | 3 - 1 - 5 - 7 | 4 - 1 - 5 - 6 | 4 - 1 - 5 - 7 |
| 7-9 | 1 - 5 - 7 - 8 | 1 - 5 - 7 - 9 | 6 - 5 - 7 - 8 |
| 10-12 | 6 - 5 - 7 - 9 | 5 - 7 - 9 - 10 | 5 - 7 - 9 - 11 |
| 13-15 | 5 - 7 - 9 - 15 | 8 - 7 - 9 - 10 | 8 - 7 - 9 - 11 |
| 16-18 | 8 - 7 - 9 - 15 | 7 - 9 - 11 - 12 | 7 - 9 - 11 - 13 |
| 19-21 | 7 - 9 - 11 - 14 | 10 - 9 - 11 - 12 | 10 - 9 - 11 - 13 |
| 22-24 | 10 - 9 - 11 - 14 | 15 - 9 - 11 - 12 | 15 - 9 - 11 - 13 |
| 25-27 | 15 - 9 - 11 - 14 | 7 - 9 - 15 - 16 | 7 - 9 - 15 - 17 |
| 28-30 | 10 - 9 - 15 - 16 | 10 - 9 - 15 - 17 | 11 - 9 - 15 - 16 |
| 31-33 | 11 - 9 - 15 - 17 | 9 - 15 - 17 - 18 | 9 - 15 - 17 - 19 |
| 34-36 | 16 - 15 - 17 - 18 | 16 - 15 - 17 - 19 | 15 - 17 - 19 - 20 |
| 37-39 | 15 - 17 - 19 - 21 | 15 - 17 - 19 - 22 | 18 - 17 - 19 - 20 |
| 40-42 | 18 - 17 - 19 - 21 | 18 - 17 - 19 - 22 | 1 - 7 - 5 - 6 |
| 43-45 | 5 - 9 - 7 - 8 | 9 - 17 - 15 - 16 | 15 - 19 - 17 - 18 |

TABLE S2. Definition of the interatomic distance index. The atom index is represented in Fig. 1(a).

| index | index of atoms for interatomic distances | | | | | | |
|---------|------------------------------------------|-------|-------|-------|-------|-------|-------|
| 1-7 | 1-6 | 1-7 | 1-8 | 1-9 | 1-10 | 1-11 | 1-12 |
| 8-14 | 1-13 | 1-14 | 1-15 | 1-16 | 1-17 | 1-18 | 1-19 |
| 15-21 | 1-20 | 1-21 | 1-22 | 2-3 | 2-4 | 2-5 | 2-6 |
| 22-28 | 2-7 | 2-8 | 2-9 | 2-10 | 2-11 | 2-12 | 2-13 |
| 29-35 | 2-14 | 2-15 | 2-16 | 2-17 | 2-18 | 2-19 | 2-20 |
| 36-42 | 2-21 | 2-22 | 3-4 | 3-5 | 3-6 | 3-7 | 3-8 |
| 43-49 | 3-9 | 3-10 | 3-11 | 3-12 | 3-13 | 3-14 | 3-15 |
| 50-56 | 3-16 | 3-17 | 3-18 | 3-19 | 3-20 | 3-21 | 3-22 |
| 57-63 | 4-5 | 4-6 | 4-7 | 4-8 | 4-9 | 4-10 | 4-11 |
| 64-70 | 4-12 | 4-13 | 4-14 | 4-15 | 4-16 | 4-17 | 4-18 |
| 71-77 | 4-19 | 4-20 | 4-21 | 4-22 | 5-8 | 5-9 | 5-10 |
| 78-84 | 5-11 | 5-12 | 5-13 | 5-14 | 5-15 | 5-16 | 5-17 |
| 85-91 | 5-18 | 5-19 | 5-20 | 5-21 | 5-22 | 6-7 | 6-8 |
| 92-98 | 6-9 | 6-10 | 6-11 | 6-12 | 6-13 | 6-14 | 6-15 |
| 99-105 | 6-16 | 6-17 | 6-18 | 6-19 | 6-20 | 6-21 | 6-22 |
| 106-112 | 7-10 | 7-11 | 7-12 | 7-13 | 7-14 | 7-15 | 7-16 |
| 113-119 | 7-17 | 7-18 | 7-19 | 7-20 | 7-21 | 7-22 | 8-9 |
| 120-126 | 8-10 | 8-11 | 8-12 | 8-13 | 8-14 | 8-15 | 8-16 |
| 127-133 | 8-17 | 8-18 | 8-19 | 8-20 | 8-21 | 8-22 | 9-12 |
| 134-140 | 9-13 | 9-14 | 9-16 | 9-17 | 9-18 | 9-19 | 9-20 |
| 141-147 | 9-21 | 9-22 | 10-11 | 10-12 | 10-13 | 10-14 | 10-15 |
| 148-154 | 10-16 | 10-17 | 10-18 | 10-19 | 10-20 | 10-21 | 10-22 |
| 155-161 | 11-15 | 11-16 | 11-17 | 11-18 | 11-19 | 11-20 | 11-21 |
| 162-168 | 11-22 | 12-13 | 12-14 | 12-15 | 12-16 | 12-17 | 12-18 |
| 169-175 | 12-19 | 12-20 | 12-21 | 12-22 | 13-14 | 13-15 | 13-16 |
| 176-182 | 13-17 | 13-18 | 13-19 | 13-20 | 13-21 | 13-22 | 14-15 |
| 183-189 | 14-16 | 14-17 | 14-18 | 14-19 | 14-20 | 14-21 | 14-22 |
| 190-196 | 15-18 | 15-19 | 15-20 | 15-21 | 15-22 | 16-17 | 16-18 |
| 197-203 | 16-19 | 16-20 | 16-21 | 16-22 | 17-20 | 17-21 | 17-22 |
| 204-210 | 18-19 | 18-20 | 18-21 | 18-22 | 20-21 | 20-22 | 21-22 |

TABLE S3. Definition of the bond angle index. The atom index is represented in Fig. 1(a). Note that the bond angles are used in cosine forms.

| index | index of atoms for bond angles | | | |
|-------|--------------------------------|----------|----------|----------|
| 1-4 | 2-1-3 | 2-1-4 | 2-1-5 | 3-1-4 |
| 5-8 | 3-1-5 | 4-1-5 | 1-5-6 | 1-5-7 |
| 9-12 | 6-5-7 | 5-7-8 | 5-7-9 | 8-7-9 |
| 13-16 | 7-9-10 | 7-9-11 | 7-9-15 | 10-9-11 |
| 17-20 | 10-9-15 | 11-9-15 | 9-11-12 | 9-11-13 |
| 21-24 | 9-11-14 | 12-11-13 | 12-11-14 | 13-11-14 |
| 25-28 | 9-15-16 | 9-15-17 | 16-15-17 | 15-17-18 |
| 29-32 | 15-17-19 | 18-17-19 | 17-19-20 | 17-19-21 |
| 33-36 | 17-19-22 | 20-19-21 | 20-19-22 | 21-19-22 |

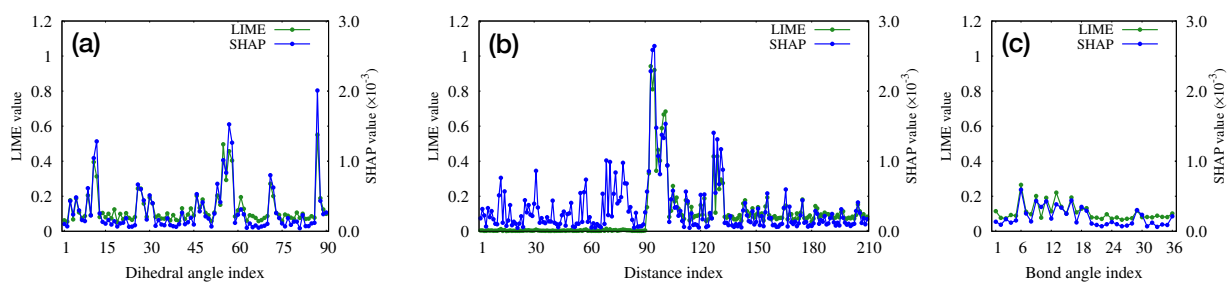


FIG. S1. Dependence of feature contribution on CV index, represented in absolute values, obtained through LIME (green) and SHAP (blue) for the neural network predictions using (i) dihedral angles + interatomic distances + bond angles. Panels (a), (b), and (c) display the index dependence of 90 dihedral angles, 210 diatomic distances, and 36 bond angles, respectively.

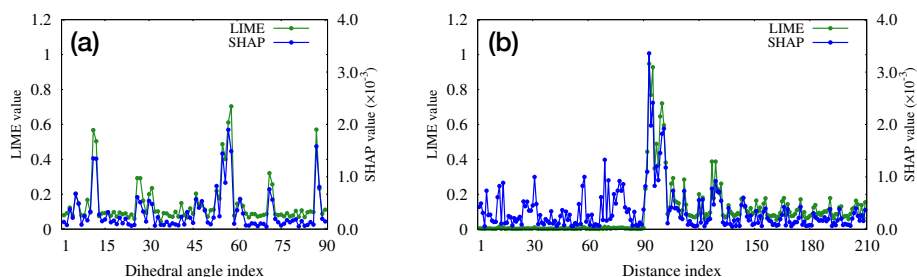


FIG. S2. Dependence of feature contribution on CV index, represented in absolute values, obtained through LIME (green) and SHAP (blue) for the neural network predictions using (ii) dihedral angles + interatomic distances. Panels (a) and (b) display the index dependence of 90 dihedral angles and 210 diatomic distances, respectively.

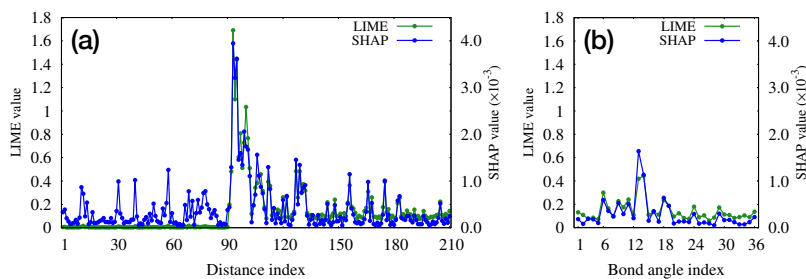


FIG. S3. Dependence of feature contribution on CV index, represented in absolute values, obtained through LIME (green) and SHAP (blue) for the neural network predictions using (iii) interatomic distances + bond angles. Panels (a) and (b) display the index dependence of 210 diatomic distances and 36 bond angles, respectively.

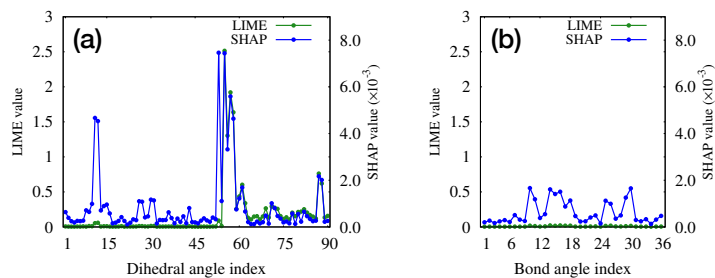


FIG. S4. Dependence of feature contribution on CV index, represented in absolute values, obtained through LIME (green) and SHAP (blue) for the neural network predictions using (iv) dihedral angles + bond angles. Panels (a) and (b) display the index dependence of 90 dihedral angles and 36 bond angles, respectively.

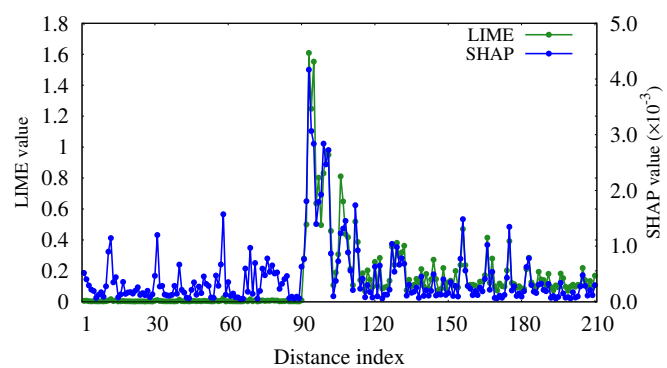


FIG. S5. Dependence of feature contribution on CV index, represented in absolute values, obtained through LIME (green) and SHAP (blue) for the neural network predictions using 210 interatomic distances.